Spin Pinning and Spin-Wave Dispersion in Nanoscopic Ferromagnetic Waveguides

Q. Wang,[1,*] B. Heinz,[1,2,*] R. Verba,[3] M. Kewenig,[1] P. Pirro,[1] M. Schneider,[1] T. Meyer,[1,4] B. Lägel,[5] C. Dubs,[6] T. Brächer,[1] and A. V. Chumak[1,†]

[1]*Fachbereich Physik and Landesforschungszentrum OPTIMAS, Technische Universität Kaiserslautern, D-67663 Kaiserslautern, Germany*

[2]*Graduate School Materials Science in Mainz, Staudingerweg 9, 55128 Mainz, Germany*

[3]*Institute of Magnetism, Kyiv 03680, Ukraine*

[4]*THATec Innovation GmbH, Augustaanlage 23, 68165 Mannheim, Germany*

[5]*Nano Structuring Center, Technische Universität Kaiserslautern, D-67663 Kaiserslautern, Germany*

[6]*INNOVENT e.V., Technologieentwicklung, Prüssingstraße 27B, 07745 Jena, Germany*

(Received 9 July 2018; revised manuscript received 5 March 2019; published 19 June 2019)

Spin waves are investigated in yttrium iron garnet waveguides with a thickness of 39 nm and widths ranging down to 50 nm, i.e., with an aspect ratio thickness over width approaching unity, using Brillouin light scattering spectroscopy. The experimental results are verified by a semianalytical theory and micromagnetic simulations. A critical width is found, below which the exchange interaction suppresses the dipolar pinning phenomenon. This changes the quantization criterion for the spin-wave eigenmodes and results in a pronounced modification of the spin-wave characteristics. The presented semianalytical theory allows for the calculation of spin-wave mode profiles and dispersion relations in nanostructures.

DOI: 10.1103/PhysRevLett.122.247202

Spin waves and their quanta, magnons, typically feature frequencies in the gigahertz to terahertz range and wavelengths in the micrometer to nanometer range. They are envisioned for the design of faster and smaller next generational information processing devices where information is carried by magnons instead of electrons [1–9]. In the past, spin-wave modes in thin films or rather planar waveguides with thickness-to-width aspect ratios $a_r = h/w \ll 1$ have been studied. Such thin waveguides demonstrate the effect of "dipolar pinning" at the lateral edges, and for its theoretical description the thin strip approximation was developed, in which only pinning of the much-larger-in-amplitude dynamic in-plane magnetization component is taken into account [10–15]. The recent progress in fabrication technology leads to the development of nanoscopic magnetic devices in which the width w and the thickness h become comparable [16–23]. The description of such waveguides is beyond the thin strip model of effective pinning, because the scale of nonuniformity of the dynamic dipolar fields, which is described as "effective dipolar boundary conditions," becomes comparable to the waveguide width. Additionally, both in-plane and out-of-plane dynamic magnetization components become involved in the effective dipolar pinning as they become of comparable amplitude. Thus, a more general model should be developed and verified experimentally. In addition, such nanoscopic feature sizes imply that the spin-wave modes bear a strong exchange character, since the widths of the structures are now comparable to the exchange length [24]. A proper description of the spin-wave eigenmodes in nanoscopic strips which considers the influence of the exchange interaction, as well as the shape of the structure, is fundamental for the field of magnonics.

In this Letter, we discuss the evolution of the frequencies and profiles of the spin-wave modes in nanoscopic waveguides where the aspect ratio a_r evolves from the thin film case $a_r \to 0$ to a rectangular bar with $a_r \to 1$. Yttrium iron garnet (YIG) waveguides with a thickness of 39 nm and widths ranging down to 50 nm are fabricated and the quasiferromagnetic resonance (quasi-FMR) frequencies within them are measured using microfocused Brillouin light scattering (BLS) spectroscopy. The experimental results are verified by a semianalytical theory and micromagnetic simulations. It is shown that a critical waveguide width exists, below which the profiles of the spin-wave modes are essentially uniform across the width of the waveguide. This is fundamentally different from the profiles in state-of-the-art waveguides of micrometer [16–19] or millimeter sizes [25,26], where the profiles are nonuniform and pinned at the waveguide edges due to the dipolar interaction. In nanoscopic waveguides, the exchange interaction suppresses this pinning due to its dominance over the dipolar interaction and, consequently, the exchange interaction defines the profiles of the spin-wave modes as well as the corresponding spin-wave dispersion characteristics.

In the experiment and the theoretical studies, we consider rectangular magnetic waveguides as shown schematically in Fig. 1(a). In the experiment, a spin-wave mode is excited by a stripline that provides a homogeneous excitation field over the sample containing various waveguides

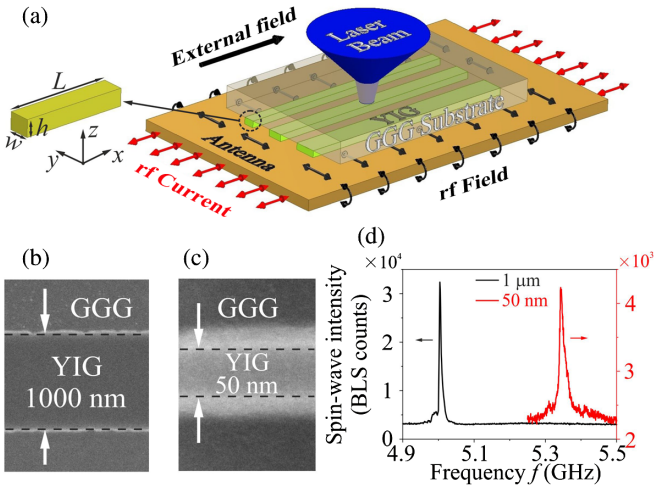

FIG. 1. (a) Sketch of the sample and the experimental configuration: a set of YIG waveguides is placed on a microstrip line to excite the quasi-FMR in the waveguides. BLS spectroscopy is used to measure the local spin-wave dynamics. (b) and (c) SEM micrograph of a 1 μm and a 50 nm wide YIG waveguide of 39 nm thickness. (d) Frequency spectra for 1 μm and 50 nm wide waveguides measured for a respective microwave power of 6 and 15 dBm.

etched from a $h = 39$ nm thick YIG film grown by liquid phase epitaxy [27] on gadolinium gallium garnet. The widths of the waveguides range from $w = 50$ nm to $w = 1$ μm with a length of 60 μm. The waveguides are patterned by Ar^+ ion beam etching using an electron-beam lithographically defined Cr/Ti hard mask and are well separated on the sample in order to avoid dipolar coupling between them [9]. The waveguides are uniformly magnetized along their long axis by an external field B (x direction). Figures 1(b) and 1(c) show scanning electron microscopy (SEM) micrographs of the largest and the narrowest waveguide studied in the experiment. The intensity of the magnetization precession is measured by microfocused BLS spectroscopy [28] (see Supplemental Material S3 [29]) as shown in Fig. 1(a). Black and red lines in Fig. 1(d) show the frequency spectra for a 1 μm and a 50 nm wide waveguide, respectively. No standing modes across the thickness were observed in our experiment, as their frequencies lie higher than 20 GHz due to the small thickness. The quasi-FMR frequency is 5.007 GHz for the 1 μm wide waveguide. This frequency is comparable to 5.029 GHz, the value predicted by the classical theoretical model using the thin strip approximation [12–14,34]. In contrast, the quasi-FMR frequency is 5.35 GHz for a 50 nm wide waveguide which is much smaller than the value of 7.687 GHz predicted by the same model. The reason is that the thin strip approximation overestimates the effect of dipolar pinning in waveguides with aspect ratio a_r close to one, for which the nonuniformity of the dynamic dipolar fields is not well localized at the waveguide edges. Additionally, in such nanoscale waveguides, the dynamic magnetization components become of the same order of magnitude and both affect the effective mode pinning, in contrast to thin waveguides, in which the in-plane magnetization component is dominant.

In order to accurately describe the spin-wave characteristic in nanoscopic longitudinally magnetized waveguides, we provide a more general semianalytical theory which goes beyond the thin strip approximation. Please note that the theory is not applicable in transversely magnetized waveguides due to their more involved internal field landscape [16]. The lateral spin-wave mode profile $\mathbf{m}_{k_x}(y)$ and frequency can be found from [35,36]

$$-i\omega_{k_x}\mathbf{m}_{k_x}(y) = \boldsymbol{\mu} \times [\hat{\boldsymbol{\Omega}}_{k_x} \cdot \mathbf{m}_{k_x}(y)], \tag{1}$$

with appropriate exchange boundary conditions, which take into account the surface anisotropy at the edges (see Supplemental Material S1 [29]). Here, $\boldsymbol{\mu}$ is the unit vector in the static magnetization direction and $\hat{\boldsymbol{\Omega}}_{k_x}$ is a tensorial Hamilton operator, which is given by

$$\hat{\boldsymbol{\Omega}}_{k_x} \cdot \mathbf{m}_{k_x}(y) = \left[\omega_H + \omega_M \lambda^2 \left(k_x^2 - \frac{d^2}{dy^2}\right)\right] \mathbf{m}_{k_x}(y) + \omega_M \int \hat{\mathbf{G}}_{k_x}(y - y') \cdot \mathbf{m}_{k_x}(y') dy'. \tag{2}$$

Here, $\omega_H = \gamma B$, B is the static internal magnetic field that is considered to be equal to the external field due to the negligible demagnetization along the x direction, $\omega_M = \gamma \mu_0 M_s$, γ is the gyromagnetic ratio. $\hat{\mathbf{G}}_{k_x}(y)$ is the Green's function (see Supplemental Material S1 [29]).

A numerical solution of Eq. (1) gives both the spin-wave profiles $\mathbf{m}_{k_x}$ and frequency ω_{k_x}. In the following, we will regard the out-of-plane component $m_z(y)$ to show the mode profiles, representatively. The profiles of the spin-wave modes can be well approximated by sine and cosine functions. In the past, it was demonstrated that in microscopic waveguides, that the fundamental mode is well fitted by the function $m_z(y) = A_0 \cos(\pi y / w_{\text{eff}})$ with the amplitude A_0 and the effective width w_{eff} [12,13]. This mode, as well as the higher modes, are referred to as "partially pinned." Pinning hereby refers to the fact that the amplitude of the modes at the edges of the waveguides is reduced. In that case, the effective width w_{eff} determines where the amplitude of the modes would vanish outside the waveguide [9,12,23]. With this effective width, the spin-wave dispersion relation can also be calculated by the analytical formula [9]

$$\omega_0(k_x) = \sqrt{[\omega_H + \omega_M(\lambda^2 K^2 + F_{k_x}^{yy})][\omega_H + \omega_M(\lambda^2 K^2 + F_{k_x}^{zz})]}, \tag{3}$$

where $K = \sqrt{k_x^2 + \kappa^2}$ and $\kappa = \pi / w_{\text{eff}}$. The tensor $\hat{F}_{k_x} = (1/2\pi) \int_{-\infty}^{\infty} (|\sigma_k|^2 / \tilde{w}) \hat{\mathbf{N}}_k dk_y$ accounts for the dynamic

demagnetization, $\sigma_k = \int_{-w/2}^{w/2} m(y) e^{-ik_y y} dy$ is the Fourier transform of the spin-wave profile across the width of the waveguide, $\tilde{w} = \int_{-w/2}^{w/2} m(y)^2 dy$ is the normalization of the mode profile $m_z(y)$.

In the following, the experiment is compared to the theory and to micromagnetic simulations. The simulations are performed using MUMAX^3 [37]. The structure is schematically shown in Fig. 1(a). The following parameters were used: the saturation magnetization $M_s = 1.37 \times 10^5$ A/m and the Gilbert damping $\alpha = 6.41 \times 10^{-4}$ were extracted from the plain film via ferromagnetic resonance spectroscopy before patterning [38]. Moreover, a gyromagnetic ratio $\gamma = 175.86$ rad/(ns T) and an exchange constant $A = 3.5$ pJ/m for a standard YIG film were assumed. An external field $B = 108.9$ mT is applied along the waveguide long axis (see Supplemental Material S2 [29]).

The central panel of Fig. 2 shows the spin-wave mode profile of the fundamental mode for $k_x = 0$, which corresponds to the quasi-FMR, in a 1 μm (a2) and 50 nm (b2) wide waveguide which has been obtained by micromagnetic simulations (red dots) and by solving Eq. (1) numerically (black lines) (higher width modes are discussed in Supplemental Material S6 [29]). The top panels (a1) and (b1) illustrate the mode profile and the local precession amplitude in the waveguide. As it can be seen, the two waveguides feature quite different profiles of their fundamental modes: in the 1 μm wide waveguide, the spins are

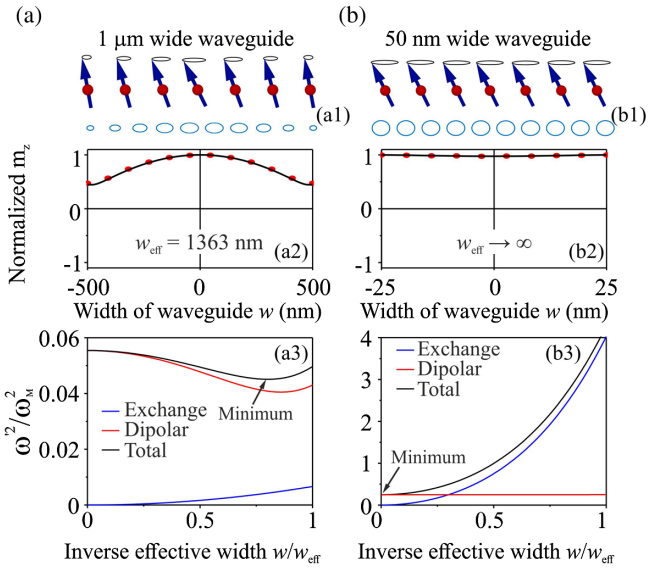

FIG. 2. Schematic of the precessing spins and simulated precession trajectories (ellipses in the second panel) and spin-wave profile $m_z(y)$ of the quasi-FMR. The profiles have been obtained by micromagnetic simulations (red dots) and by the quasianalytical approach (black lines) for an (a) 1 μm and a (b) 50 nm wide waveguide. Bottom panel: Normalized square of the spin-wave eigenfrequency ω'^2/ω_M^2 as a function of w/w_{eff} and the relative dipolar and exchange contributions.

partially pinned and the amplitude of m_z at the edges of the waveguide is reduced. This still resembles the cosinelike profile of the lowest width mode $n = 0$ that has been well established in investigations of spin-wave dynamics in waveguides on the micron scale [19,23,39] and that can be well described by the simple introduction of a finite effective width $w_{\text{eff}} > w$ ($w_{\text{eff}} = w$ for the case of full pinning). In contrast, the spins at the edges of the narrow waveguide are completely unpinned and the amplitude of the dynamic magnetization m_z of the lowest mode $n = 0$ is almost constant across the width of the waveguide, resulting in $w_{\text{eff}} \to \infty$.

To understand the nature of this depinning, it is instructive to consider the spin-wave energy as a function of the geometric width of the waveguide normalized by the effective width w/w_{eff}. This ratio corresponds to some kind of pinning parameter taking values in between 1 for the fully pinned case and 0 for the fully unpinned case. The system will choose the mode profile which minimizes the total energy. This is equivalent to a variational minimization of the spin-wave eigenfrequencies as a function of w/w_{eff}. To illustrate this, the lower panels of Figs. 2(a3) and 2(b3) show the normalized square of the spin-wave eigenfrequencies ω'^2/ω_M^2 for the two different widths as a function of w/w_{eff}. Here, ω'^2 refers to a frequency square, not taking into account the Zeeman contribution $(\omega_H^2 + \omega_H \omega_M)$, which only leads to an offset in frequency. The minimum of ω'^2 is equivalent to the solution with the lowest energy corresponding to the effective width w_{eff}. In addition to the total ω'^2 (black), also the individual contributions from the dipolar term (red) and the exchange term (blue) are shown, which can only be separated conveniently from each other if the square of Eq. (3) is considered for $k_x = 0$. The dipolar contribution is nonmonotonic and features a minimum at a finite effective width w_{eff}, which can clearly be observed for $w = 1$ μm. The appearance of this minimum, which leads to the effect known as "effective dipolar pinning" [13,14], is a result of the interplay of two tendencies: (i) an increase of the volume contribution with increasing w/w_{eff}, as for common Damon-Eshbach spin waves, and (ii) a decrease of the edge contribution when the spin-wave amplitude at the edges vanishes ($w/w_{\text{eff}} \to 1$). This minimum is also present in the case of a 50 nm wide waveguide (red line), even though this is hardly perceivable in Fig. 2(b3) due to the scale. In contrast, the exchange leads to a monotonic increase of frequency as a function of w/w_{eff}, which is minimal for the unpinned case, i.e., $w/w_{\text{eff}} = 0$ implying $w_{\text{eff}} \to \infty$, when all spins are parallel. In the case of the 50 nm waveguide, the smaller width and the corresponding much larger quantized wave number in the case of pinned spins would lead to a much larger exchange contribution than this is the case for the 1 μm wide waveguide (please note the vertical scales). Consequently, the system avoids pinning and the solution with lowest energy is situated at

$w/w_{\mathrm{eff}} = 0$. In contrast, in the 1 μm wide waveguide, the interplay of dipolar and exchange energy implies that energy is minimized at a finite w/w_{eff}. The top panel of Fig. 2(b1) shows an additional feature of the narrow waveguide: as the aspect ratio of the waveguides approaches unity, the ellipticity of precession, a well-known feature of micron-sized waveguides which still resemble a thin film [23,40], vanishes and the precession becomes nearly circular. Also, in nanoscale waveguides, the ellipticity is constant across the width, while in the 1 μm wide waveguide it can be different at the waveguide center and near its edges. Please note that the pinning phenomena and ellipticity of precession also influence the spin-wave lifetime which is described in the Supplemental Material S5 [29].

As it is evident from the lower panel of Fig. 2, the pinning and the corresponding effective width have a large influence on the spin-wave frequency. This allows for an experimental verification of the presented theory, since the frequency of partially pinned spin-wave modes would be significantly higher than in the unpinned case. Black squares in Fig. 3(a) summarize the dependence of the frequency of the quasi-FMR measured for different widths of the YIG waveguides. The magenta line shows the expected frequencies assuming pinned spins, the blue (dashed) line gives the resonance frequencies extrapolating the formula conventionally used for micron-sized waveguides [34] to the nanoscopic scenario, and the red line gives the result of the theory presented here, together with simulation results (green dashed line). As it can be seen, the experimentally observed frequencies can be well reproduced if the real pinning conditions are taken into account.

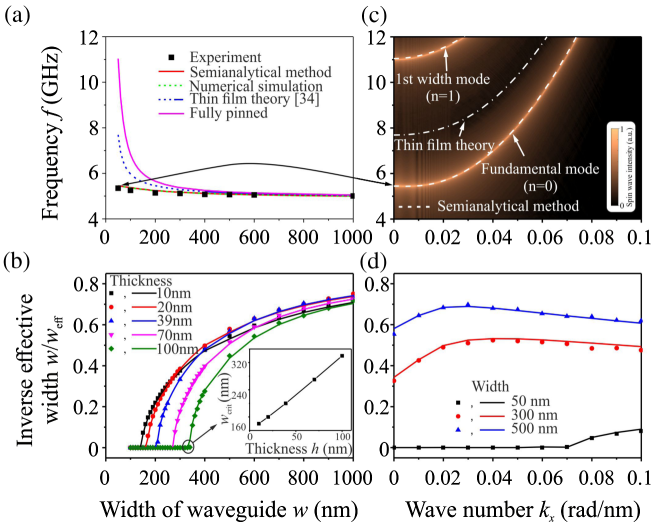

FIG. 3. (a) Experimentally determined resonance frequencies (black squares) together with theoretical predictions and micromagnetic simulations. (b) Inverse effective width w/w_{eff} as a function of the waveguide width. The inset shows the critical width (w_{crit}) as a function of thickness h. (c) Spin-wave dispersion relation of the first two width modes from micromagnetic simulations (color code) and theory (dashed lines). (d) Inverse effective width w/w_{eff} as a function of the spin-wave wave number k_x for different thicknesses and waveguide widths, respectively.

As has been discussed along with Fig. 2, the unpinning occurs when the exchange interaction contribution becomes so large that it compensates the minimum in the dipolar contribution to the spin-wave energy. Since the energy contributions and the demagnetization tensor change with the thickness of the investigated waveguide, the critical width below which the spins become unpinned is different for different waveguide thicknesses. This is shown in Fig. 3(b), where the inverse effective width w/w_{eff} is shown for different waveguide thicknesses. Symbols are the results of micromagnetic simulations, lines are calculated semianalytically. As can be seen from the figure, the critical width linearly increases with increasing thickness. This is summarized in the inset, which shows the critical width (i.e., the maximum width for which $w/w_{\mathrm{eff}} = 0$) as a function of thickness. The critical widths for YIG, Permalloy, CoFeB, and Heusler compound ($Co_2Mn_{0.6}Fe_{0.4}Si$) with different thicknesses are given in the Supplemental Material S9 [29]. A simple empirical linear formula is found by fitting the critical widths for different materials in a wide range of thicknesses:

$$w_{\mathrm{crit}} = 2.2h + 6.7\lambda, \tag{4}$$

where h is the thickness of the waveguide and λ is the exchange length. Please note that additional simulations with rough edges and a more realistic trapezoidal cross section of the waveguides are also provided in the Supplemental Material S7, S8 [29]. The results show that these effects have a small impact on the critical width.

Up to now, the discussion was limited to the special case of $k_x = 0$. In the following, the influence of a finite wave vector will be addressed. The spin-wave dispersion relation of the fundamental ($n = 0$) mode obtained from micromagnetic simulations (color code) together with the semianalytical solution (white dashed line) are shown in Fig. 3(c) for the YIG waveguide of $w = 50$ nm width. The figure also shows the low-wave-number part of the dispersion of the first width mode ($n = 1$), which is pushed up significantly in frequency due to its large exchange contribution. Both modes are described accurately by the quasianalytical theory. As it is described above, the spins are fully unpinned in this particular case. In order to demonstrate the influence of the pinning conditions on the spin-wave dispersion, a hypothetic dispersion relation for the case of partial pinning is shown in the figure with a dash-dotted white line (the case of $w/w_{\mathrm{eff}} = 0.63$ is considered that would result from the usage of the thin strip approximation [12]). One can clearly see that the spin-wave frequencies in this case are considerably higher. Figure 3(d) shows the inverse effective width w/w_{eff} as a function of the wave number k_x for three exemplary

waveguide widths of $w = 50$, 300, and 500 nm. As it can be seen, the effective width and, consequently, the ratio w/w_{eff} shows only a weak nonmonotonic dependence on the spin-wave wave number in the propagation direction. This dependence is a result of an increase of the inhomogeneity of the dipolar fields near the edges for larger k_x, which increases pinning [14], and of the simultaneous decrease of the overall strength of dynamic dipolar fields for shorter spin waves. Please note that the mode profiles are not only important for the spin-wave dispersion. The unpinned mode profiles will also greatly improve the coupling efficiency between two adjacent waveguides [9,41–43].

In conclusion, the quasi-FMR of individual wires with widths ranging from 1 μm down to 50 nm are studied by means of BLS spectroscopy. A difference in the quasi-FMR frequency between experiment and the prediction by the classical thin strip theory is found for 50 nm wide waveguides. A semianalytical theory accounting for the nonuniformity of both in-plane and out-of-plane dynamic demagnetization fields is presented and is employed together with micromagnetic simulations to investigate the spin-wave eigenmodes in nanoscopic waveguides with aspect ratio a_r approaching unity. It is found that the exchange interaction is getting dominant with respect to the dipolar interaction, which is responsible for the phenomenon of dipolar pinning. This mediates an unpinning of the spin-wave modes if the width of the waveguide becomes smaller than a certain critical value. This exchange unpinning results in a quasiuniform spin-wave mode profile in nanoscopic waveguides in contrast to the cosinelike profiles in waveguides of micrometer widths and in a decrease of the total energy and, thus, frequency, in comparison to the fully or the partially pinned case. Our theory allows us to calculate the mode profiles as well as the spin-wave dispersion, and to identify a critical width below which fully unpinned spins need to be considered. The presented results provide valuable guidelines for applications in nanomagnonics where spin waves propagate in nanoscopic waveguides with aspect ratios close to one and lateral sizes comparable to the sizes of modern CMOS technology.

The authors thank Burkard Hillebrands and Andrei Slavin for valuable discussions. This research has been supported by ERC Starting Grant No. 678309 MagnonCircuits and by the DFG through the Collaborative Research Center SFB/TRR-173 "Spin + X" (Projects B01) and through the Project No. DU 1427/2-1. R. V. acknowledges support from the Ministry of Education and Science of Ukraine, Project No. 0118U004007.

*These authors have contributed equally to this work.
†Corresponding author.
chumak@physik.uni-kl.de

[1] A. V. Chumak, V. I. Vasyuchka, A. A. Serga, and B. Hillebrands, Nat. Phys. **11**, 453 (2015).
[2] V. V. Kruglyak, S. O. Demokritov, and D. Grundler, J. Phys. D **43**, 264001 (2010).
[3] C. S. Davies, A. Francis, A. V. Sadovnikov, S. V. Chertopalov, M. T. Bryan, S. V. Grishin, D. A. Allwood, Y. P. Sharaevskii, S. A. Nikitov, and V. V. Kruglyak, Phys. Rev. B **92**, 020408(R) (2015).
[4] A. Khitun, M. Bao, and K. L. Wang, J. Phys. D **43**, 264005 (2010).
[5] M. Schneider, T. Brächer, V. Lauer, P. Pirro, D. A. Bozhko, A. A. Serga, H. Yu. Musiienko-Shmarova, B. Heinz, Q. Wang, T. Meyer, F. Heussner, S. Keller, E. Th. Papaioannou, B. Lägel, T. Löber, V. S. Tiberkevich, A. N. Slavin, C. Dubs, B. Hillebrands, and A. V. Chumak, arXiv:1612.07305.
[6] M. Krawczyk and D. Grundler, J. Phys. Condens. Matter **26**, 123202 (2014).
[7] S. Wintz, V. Tiberkevich, M. Weigand, J. Raabe, J. Lindner, A. Erbe, A. Slavin, and J. Fassbender, Nat. Nanotechnol. **11**, 948 (2016).
[8] T. Brächer and P. Pirro, J. Appl. Phys. **124**, 152119 (2018).
[9] Q. Wang, P. Pirro, R. Verba, A. Slavin, B. Hillebrands, and A. V. Chumak, Sci. Adv. **4**, e1701517 (2018).
[10] G. T. Rado and J. R. Weertamn, J. Phys. Chem. Solids **11**, 315 (1959).
[11] R. W. Doman and J. R. Eshbach, J. Phys. Chem. Solids **19**, 308 (1961).
[12] K. Yu. Guslienko, S. O. Demokritov, B. Hillebrands, and A. N. Slavin, Phys. Rev. B **66**, 132402 (2002).
[13] K. Yu. Guslienko and A. N. Slavin, Phys. Rev. B **72**, 014463 (2005).
[14] K. Yu. Guslienko and A. N. Slavin, J. Magn. Magn. Mater. **323**, 2418 (2011).
[15] R. E. Arias, Phys. Rev. B **94**, 134408 (2016).
[16] T. Brächer, O. Boulle, G. Gaudin, and P. Pirro, Phys. Rev. B **95**, 064429 (2017).
[17] V. E. Demidov and S. O. Demokrikov, IEEE Trans. Magn. **51**, 0800215 (2015).
[18] F. Ciubotaru, T. Devolder, M. Manfrini, C. Adelmann, and I. P. Radu, Appl. Phys. Lett. **109**, 012403 (2016).
[19] P. Pirro, T. Brächer, A. V. Chumak, B. Lägel, C. Dubs, O. Surzhenko, P. Görnert, B. Leven, and B. Hillebrands, Appl. Phys. Lett. **104**, 012402 (2014).
[20] M. Mruczkiewicz, P. Graczyk, P. Lupo, A. Adeyeye, G. Gubbiotti, and M. Krawczyk, Phys. Rev. B **96**, 104411 (2017).
[21] A. Haldar and A. O. Adeyeye, ACS Nano **10**, 1690 (2016).
[22] R. Verba, V. Tiberkevich, E. Bankowski, T. Meitzler, G. Melkov, and A. Slavin, Appl. Phys. Lett. **103**, 082407 (2013).
[23] T. Brächer, P. Pirro, and B. Hillebrands, Phys. Rep. **699**, 1 (2017).
[24] G. Abo, Y. Hong, J. Park, J. Lee, W. Lee, and B. Choi, IEEE Trans. Magn. **49**, 4937 (2013).
[25] M. Vogel, A. V. Chumak, E. H. Waller, T. Langer, V. I. Vasyuchka, B. Hillebrands, and G. Von Greymann, Nat. Phys. **11**, 487 (2015).
[26] A. A. Serga, A. V. Chumak, and B. Hillebrands, J. Phys. D **43**, 264002 (2010).
[27] C. Dubs, O. Surzhenko, R. Linke, A. Danilewsky, U. Brückner, and J. Dellith, J. Phys. D **50**, 204005 (2017).

[28] T. Sebastian, K. Schultheiss, B. Obry, B. Hillebrands, and H. Schultheiss, Front. Phys. **3**, 35 (2015).
[29] See Supplemental Material at http://link.aps.org/supplemental/10.1103/PhysRevLett.122.247202 for details of numerical solution and micromagnetic simulations, which includes Refs. [30–33].
[30] V. V. Kruglyak, O. Yu. Gorobets, Yu. I. Gorobets, and A. N. Kuchko, J. Phys. Condens. Matter **26**, 406001 (2014).
[31] D. D. Stancil, J. Appl. Phys. **59**, 218 (1986).
[32] D. D. Stancil and A. Prabhakar, *Spin Waves: Theory and Applications* (Springer, New York, 2009).
[33] R. Verba, V. Tiberkevich, and A. Slavin, Phys. Rev. B **98**, 104408 (2018).
[34] B. A. Kalinikos and A. N. Slavin, J. Phys. C **19**, 7013 (1986).
[35] R. Verba, G. Melkov, V. Tiberkevich, and A. Slavin, Phys. Rev. B **85**, 014427 (2012).
[36] R. Verba, Ukr. J. Phys. **58**, 758 (2013).
[37] A. Vansteenkiste, J. Leliaert, M. Dvornik, M. Helsen, F. Garcia-Sanchez, and B. Van Waeyenberge, AIP Adv. **4**, 107133 (2014).
[38] I. S. Maksymov and M. Kostylev, Physica (Amsterdam) **69E**, 253 (2015).
[39] M. B. Jungfleisch, W. Zhang, W. Jiang, H. Chang, J. Sklenar, S. M. Wu, J. E. Pearson, A. Bhattacharya, J. B. Ketterson, M. Wu, and A. Hoffman, J. Appl. Phys. **117**, 17D128 (2015).
[40] A. G. Gurevich and G. A. Melkov, *Magnetization Oscillations and Waves* (CRC Press, New York, 1996).
[41] A. V. Sadovnikov, E. N. Beginin, S. E. Sheshukova, D. V. Romanenko, Yu. P. Sharaevskii, and S. A. Nikitov, Appl. Phys. Lett. **107**, 202405 (2015).
[42] A. V. Sadovnikov, A. A. Grachev, S. E. Sheshukova, Yu. P. Sharaevskii, A. A. Serdobintsev, D. M. Mitin, and S. A. Nikitov, Phys. Rev. Lett. **120**, 257203 (2018).
[43] A. V. Sadovnikov, S. A. Odintsov, E. N. Beginin, S. E. Sheshukova, Yu. P. Sharaevskii, and S. A. Nikitov, Phys. Rev. B **96**, 144428 (2017).